19e Journées de l'Hydrodynamique
26 – 28 novembre 2024, Nantes

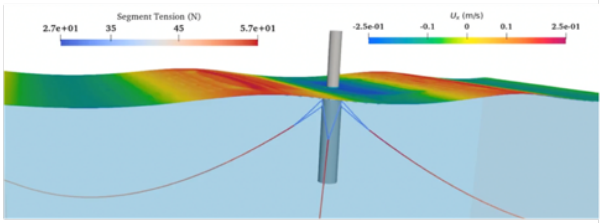

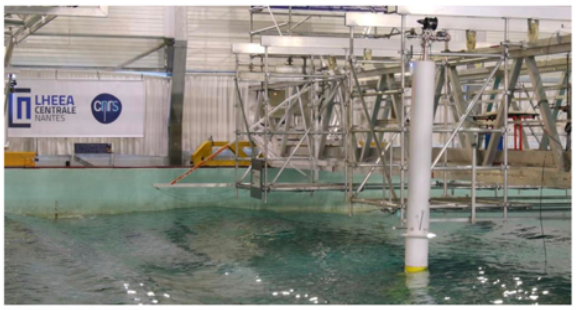

OPTIMISATION MULTI-FIDELITE NUMERIQUE/EXPERIMENTALE DES LOIS DE CALAGE D'UN PROPULSEUR CYCOIDAL

MULTI-FIDELITY NUMERICAL/EXPERIMENTAL OPTIMIZATION OF CYCLOIDAL PROPELLER PITCHING LAWS

G. FASSE[(1)], F. HAUVILLE[(2)], M. SACHER[(1)]
guillaume.fasse@ensta-bretagne.fr ; frederic.hauville@ecole-navale.fr ; matthieu.sacher@ensta-bretagne.fr

[(1)]ENSTA Bretagne, CNRS UMR 6027, IRDL, 2 rue Francois Verny, 29806 Brest Cedex9, France
[(2)]Naval Academy Research Institute (IRENav), BCRM Brest, CC600, 29240 Brest Cedex9, France

Résumé

La propulsion cycloidale promet une utilisation intéressante sur les navires du futur. Ses capacités d'opération à basse vitesse d'avance, cas du propulseur Voith-Schneider, et à haute vitesse d'avance avec une cinématique des pales différente (cas du propulseur Lipp ou ADVPropulse) en font un système de propulsion polyvalent et efficient pour une grande plage de fonctionnement. En outre, sa capacité à orienter la poussée sur 360° de façon quasi-instantannée fait de cette technologie un choix de propulseur prometteur pour contrôler la dérive des navires à assistance vélique.

Dans ce papier, les auteurs utilisent une plateforme expérimentale simulant le fonctionnement des propulseurs cycloidaux et qui permet en outre de recourir à l'optimisation des lois de calage grâce à une architecture électrique de commande des pales. Une paramétrisation adéquate des lois de calage apporte des gains conséquents sur les performances globales du propulseurs en fonction du ou des objectifs fixés durant l'optimisation. Les travaux récents ont montré un gain de 10 à 20% sur la poussée et le rendement grâce à la dissymétrie des lois optimisées en comparaison avec des lois sinusoidales classiquement utilisées sur les propulseurs à architecture de commande de pale mécanique.

L'étude présentée ici porte sur l'amélioration du processus d'optimisation en faisant recours à un métamodèle issu des résultats de calculs CFD, afin de converger plus rapidement vers l'optimum et ainsi de réduire le coût global de l'optimisation en utilisant une approche multi-fidélité numérique-expérience. En effet, l'utilisation du premier niveau de fidélité (numérique) permet de réduire le nombre d'évaluation du modèle haute fidélité (expérience). L'impact sur les résultats d'optimisation avec l'ajout de ce niveau de fidélité modifie la forme du front de pareto, mais influence peu la forme des lois optimales.

Enfin, à travers des optimisations pour plusieurs valeurs de λ, ces travaux permettent d'analyser la forme des lois de calages optimales pour plusieurs modes d'opérations. Ainsi en mode cycloidal, pour de faibles valeurs de λ, il est nécéssaire de changer la loi de calage pour modifier la poussée et conserver des performances optimales.

Summary

Cycloidal propulsion promises interesting application for the next generation of ships. Its operating capabilities at low ship speed, as the well known Voith-Schneider Propeller, and at high ship speed, as the Lipp propeller or ADVPropulse system, result on a versatile and efficient propeller for a wide range of operation. Moreover, cycloidal propulsion is characterized by the ability of rotating the thrust over 360° quasi-instantaneously. This feature makes this technology an suitable choice for wind assisted ship propulsion as it can balance the possible leeway of the ship.

Through this paper, authors pursue investigation of pitch law optimization using experimental cross flow platform developed these last years. Thanks to an electric blade control architecture, this platform allows users to rely on blade pitch optimization using surrogate models. The fitted parameterization of the pitch law involves large increase of the global propeller performances according to the optimization objectives. The latest results reveal 10 to 20% increase of the thrust and efficiency of optimized pitching laws versus sinusoidal pitching laws classically used by mechanical cycloidal propeller.

In the continuity of pitch optimization, this paper investigates the use of a multi-fidelity approach by integrating CFD simulation results as additional meta-model and thus decrease the optimization cost. Indeed, the use of lower fidelity level (CFD) decreases the number of evaluation of the higher fidelity level (experimental) during the optimization process. Impact of the multi-fidelity process modifies the predicted Pareto front from optimisation results. But it doesn't affect the optimal pitching law shape.

Lastly, through the optimizations for various λ values, this study provides an analyse of the optimal pitching law for many operating modes. Results reveal that for low λ values, modifying the pitching law is essential to change the thrust and keep optimal performances.

I – Introduction

Cycloidal propulsion is divided into two main operation modes for which blade motion are significantly different: the cycloid motion which is used for low advance speed vessels and trochoid motion which allows the ship to reach higher speed. Cycloidal motion is charaterized by the rotation of the blades around the tangent to the rotor whereas for the trochoid motion, the blades are rotating around the advance speed direction. The advance value λ, is defined as the ratio of the advance speed V_A to the blade peripheral speed ωR, where R is the orbital radius of the propulsor and ω is the rotational speed (in rad/s). When λ <1, the most suitable motion is the cycloidal motion whereas when λ >1 it is the trochoidal motion. These blade kinematics are widely discussed in [2, 18, 5]. Since now, existing cycloidal propulsion technologies use a mechanical blade command, as the well-known Voith Schneider Propeller which use a cycloidal motion, or Lipp and ADVPropulse systems which use a trochoidal motion.

The development of the SHIVA platform these last years [5, 6] promises a wide range of study for cycloidal propulsion optimization. Indeed, thanks to individual servo-motors which actuates independently each blades, authors can test and optimize all type of blade

kinematic for both cycloidal and trochoidal modes. This experimental platform is also equipped with many sensors to measure performance of each pitch law tested. All the features of the platform are widely explained in [5]. Growing use of CFD calculation to study cycloidal propulsion and determining their performances is also noticeable as in [12].

The specificity of the study presented here is to perform cycloidal pitch law optimization using both experimental and numerical models to evaluate the performances. This process, called multi-fidelity, has already been used but mainly with different numerical models [20]. The innovation comes from the use of simultaneously numerical and experimental evaluation in the optimization procedure. The multi-fidelity process allows the use of more parameters on the pitch law definition thanks to the lower number of evaluation required (in comparison with a single fidelity process). Nonetheless, the use of multi-fidelity process also allows authors to prepare various optimization for many λ values by evaluate performance of numerical points of optimization before the experimental test week.

This paper describes first the two models used for the optimization: the experimental test-bench SHIVA and the numerical CFD model. Then the optimization problem and the pitch law parameterization are presented. The optimization method is then widely explained. Finally, the results of multi-fidelity optimization for three different operating points λ and for both cycloidal and trochoidal mode are discussed and compared.

II – Multi-models approach

As the optimization problem presented in this study is based on two distinct models (experiments and numerical calculations), both of them require to be correctly defined.

The experimental setup is first described in Section II – 1. Then, Section II – 2 defines the CFD numerical model implementation and validation. Finally, Section II – 3 deals with the optimization problem and the adapted parameterization method.

II – 1 Experimental setup

To perform the optimizations, the experimental blade controlled cross-flow platform SHIVA is operating at the IFREMER wave and current flume tank. Figure 1 gives an overview of the platform, its positioning in the flume tank and the associated reference frames. For interested readers, the technical features and control commands of the experimental platform, along with its instrumentation and the post-processing of experimental signals, are thoroughly detailed in [5]. For the present experimental campaign, the radius of the rotary triangular frame is set at $R = 0.4$m, and blades are NACA0018 profile with a chord length $c = 0.15$m, and a wet span of $b = 0.92$m. The embedded blade load-cell is configured for a measuring range of 900N on the blade normal direction F_{N_b} and 200N on the blade tangential direction F_{T_b}. The tank speed V_{tank} varies from 0.2m/s at λ=0.2 to 0.3m/s for λ=$\{0.375, 0.5\}$ and the rotational speed ω of the platform is adapted according the definition of $\lambda = \frac{V}{\omega R}$.

Concerning measurements procedure, as detailed in [6], the data recording is proceeding during 20 rotations of the platform after waiting that the tank flow is fully established. The post-process of the experimental signals consists of a series of signal treatment (filter, trigger-tunning, no-load signal subtraction, transformation matrix, turn trimming) and the total blade forces from the 3 blades are constructed from the embedded load-cell blade forces. Averages and coefficient are then calculated to compute the objective functions

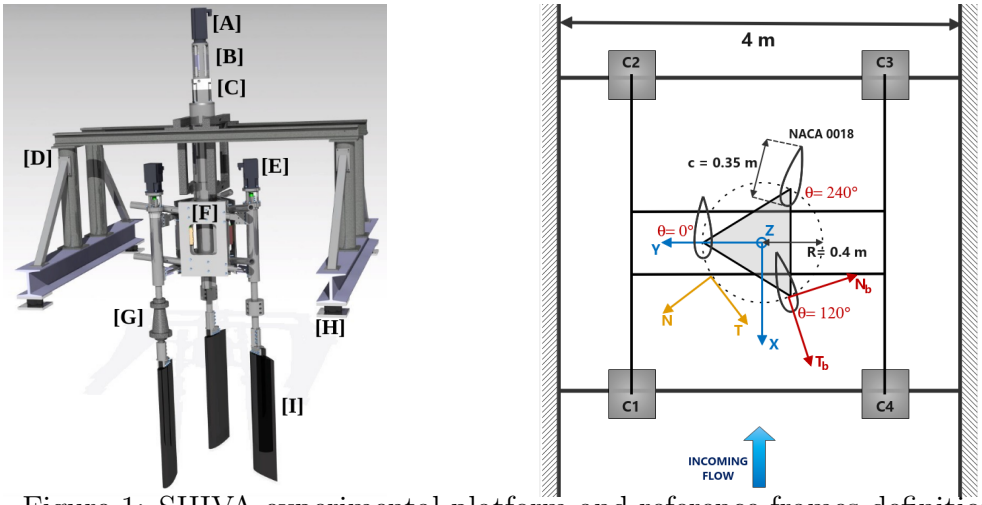

Figure 1: SHIVA experimental platform and reference frames definition.

of the optimization process. Finally any new optimized pitch law is directly transferred from the optimization computer at the edge of the tank to the platform thanks to the command Human Machine Interface.

II – 2 Numerical model

Numerical results presented in this paper are provided from 2D CFD calculations using FINE/Marine software (version 11.2). The domain, illustrated in Figure 2, consists of a rectangular hexahedral mesh, with a length of 150m and a width of 4m corresponding of the experimental tank width. The cycloidal propeller is represented by the three 0.15m chord blade profiles, rotating in the rectangular mesh. A dual sliding mesh method is used to both, rotate the main rotor domain from the fixed rectangular domain, and rotate each blade domain from the rotor domain (these sliding domains are highlighted in blue in Figure 2) .

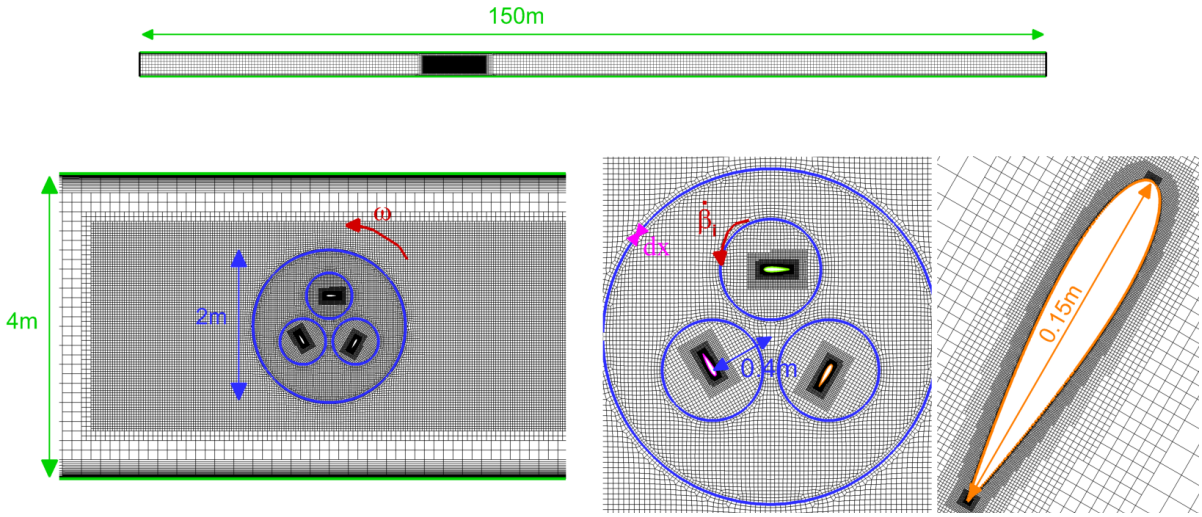

Figure 2: CFD mesh illustration with the different sliding domains.

The rotor domain rotates at the rotational speed ω whereas each blade domain rotates at the pitch angle speed $\dot{\beta}_{1,2,3}$, thanks to a dynamic library compiled from the dedicated pitch laws. Subdivision levels are used to refine the mesh near the cycloidal rotor and its

wake, and additional subdivision levels are used to refine the mesh close to the blades. A total of 68,250 cells are generated for the coarse mesh. As boundary conditions, a velocity inlet is set on the left domain side, whereas pressure outlet is imposed on the right side of the rectangular domain. Lateral boundaries of the rectangular domain (highlighted in green in Figure 2) are specified as wall-functions conditions and mesh refinements are applied. Finally, blades are specified as walls with no-slip conditions for which the viscous layer is resolved with a minimal cell size corresponding to $y^+ = 1$. The K-Omega STT turbulence model is used to simulate the small eddy scale. Concerning numerical parameters, spatial and temporal discretization use AVLSMART scheme, which is conventionally used for the FINE/Marine ISIS-CFD solver. Finally, the timestep is set to ensure a Courant number CFL below one, with a maximum of 25 nonlinear iterations per timestep, and a total number of timestep corresponding to 20 rotations of the rotor domain.

To verify the mesh sensitivity, a finer mesh is presently provided. It has been generated with a number of cells up to 650,000 by doubling the number of cells in the initial rectangular domain, and therefore the following subdivision refinements. Figure 3 compares the blade force coefficients between experiments and CFD calculations for the two coarse and fine mesh, for the $e = 0.8$ cycloidal law, which is commonly used for Voith-Schneider Propeller systems. This pitch law is symmetrical front/downstream and is generated by an eccentricity parameter equal to 0.8 (the pitch law is illustrated on Figure 9 and its definition is given by [18]).

Results of blade force coefficients show that both meshes are in good agreement with experiments, especially when $\theta \in [0°,270°]$. It should also be noted that peak transverse force, for $\theta \approx 180°$, is overestimated, but its location is well captured by numerical models. On the downstream half, differences between numerical and experimental results appears for $\theta \approx 300°$. Nonetheless, since both meshes align well with the experimental results, the coarse mesh is selected for the multi-fidelity optimizations to lower computational costs.

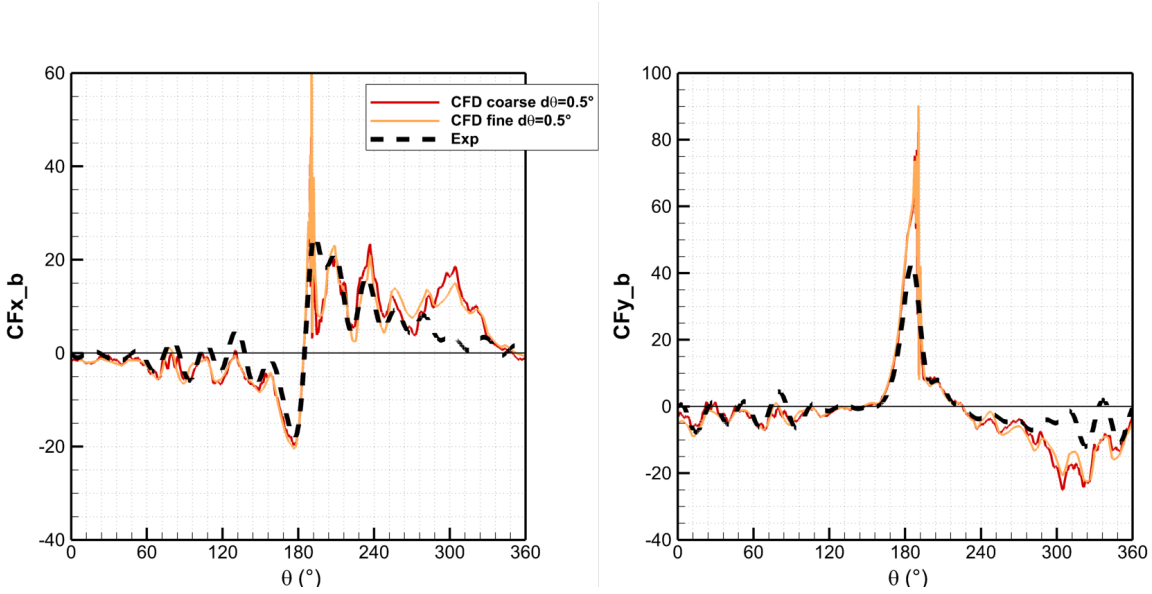

Figure 3: Comparison of different mesh size CFD results with the experimental measurement on the blade thrust (left) and blade side force (right) coefficients. Operating conditions: $e = 0.8$ pitch law, $\lambda = 0.375$, $V = 0.2$ m/s, $\omega = 1.33$ rad/s.

Time step is another CFD parameter that has a major impact on the accuracy of

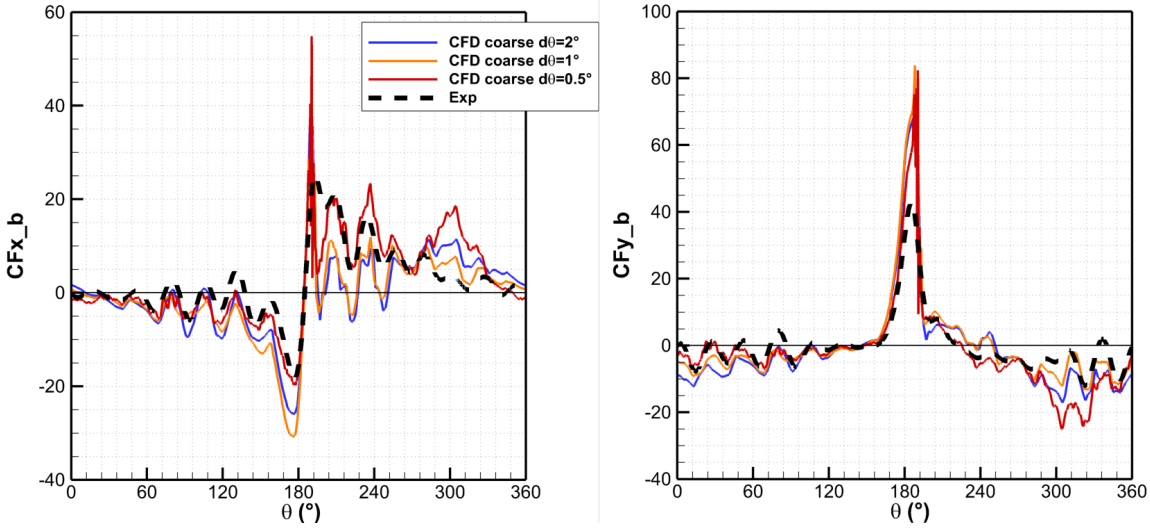

Figure 4: Comparison of different azimuth steps $d\theta$ CFD results with the experimental measurement on the blade thrust (left) and blade side force (right) coefficients. Operating conditions: $e = 0.8$ pitch law, $\lambda = 0.375$, $V = 0.2$ m/s, $\omega = 1.33$ rad/s.

results. To study its sensitivity, the timestep is expressed as azimuth step $d\theta = \omega dt$, and the Courant number is expressed as function of the cell size dx located at the main rotor domain interface: $CFL_\omega = R\frac{d\theta}{dx}$. By adjusting the timestep, and thus, the azimuth step, the Courant number is varying.

Figure 4 presents the $d\theta$ sensitivity for the coarse mesh and provides the blade-force coefficients results. The case with the lower azimuth step $d\theta = 0.5°$ fits the experiments very well especially on the first half of rotation and for the blade reversal. Higher azimuth step show a lack of time resolution to correctly capture the flow development, especially after the blade reversal $\theta \in [180°,270°]$. For the optimization procedure, all simulations are then performed with a timestep corresponding to $d\theta = 0.5°$.

Since optimization is also conducted at high lambda values for the trochoidal mode, the same validation procedure is applied to a sinusoidal pitch law with a maximum amplitude of 30°. The same results are obtained but are not presented to conserve space in the paper.

II – 3 Parametric and problem definition

The hydrodynamic performance of the cycloidal propeller is optimised by determining the optimal blade pitch laws over a range of operating conditions. To achieve this, a parametric model, inspired from [1, 6], of the pitch laws is adopted. For trochoidal mode, it consists of defining $\phi = f(\theta)$ as a cubic Hermite spline. In particular, the spline interpolates two control points (θ_1,ϕ_1) and (θ_2,ϕ_2), imposing constraints on derivatives: $\frac{d\phi}{d\theta}(\theta = \theta_1) = \frac{d\phi}{d\theta}(\theta = \theta_2) = 0$. To ensure C1 continuity of the blade pitch laws, the two control points are repeated in $\theta = \pm 2\pi$. For cycloidal mode, the method is similar with $\beta = f(\theta)$, considering (β_1,β_2) instead of (ϕ_1,ϕ_2). Examples of parametric blade pitch laws are provided in Figure 5 for cycloidal and trochoidal modes. The four-parameter setup, $(\theta_1,\phi_1,\theta_2,\phi_2)$ or $(\theta_1,\beta_1,\theta_2,\beta_2)$, allows fine and non-symmetrical control of the maximum amplitudes and associated azimuthal locations of the law. In addition to offering a wide variety of generated laws, this parametric model preserves the fact of having $\phi(\theta = 0) \neq 0$

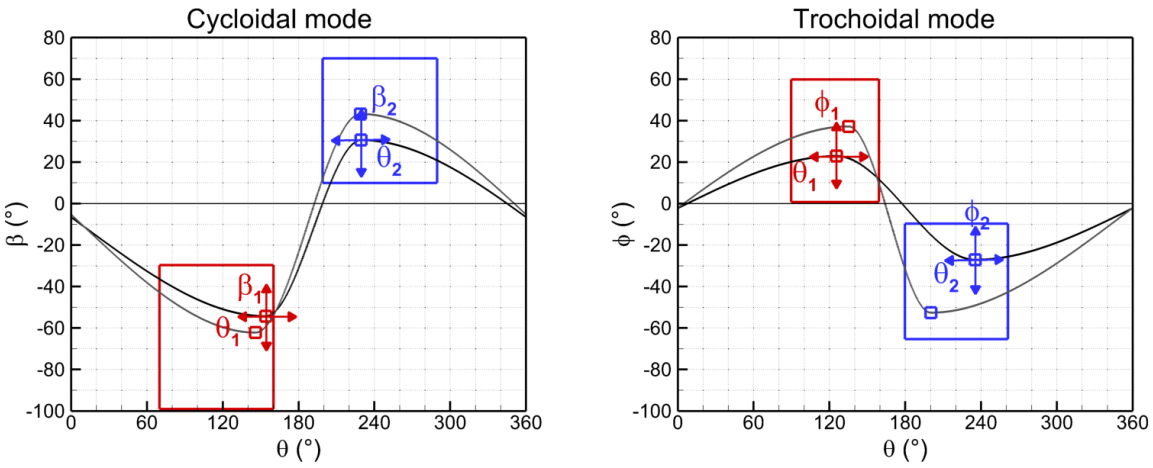

Figure 5: Parametric model of cycloidal pitch laws at the left and trochoidal pitch laws at the right.

or $\beta(\theta = 0) \neq 0$. Such properties are critical to maximizing the propeller's performance [6].

In the present work, hydrodynamic performances of the vertical axis propeller are optimized over multiple operating points. An operating point means a fixed λ, and hydrodynamic performances are represented as objective functions. In other words, several optimizations are presently solved at different λ values, where objective functions, to be optimized, are dependent on the four-parameter pitch law setup. In particular, two objective functions are considered:

$$\overline{C_{F_x}} = \frac{\overline{F_{x_{tot}}}}{0.5\rho S V^2} \qquad \text{and} \qquad \overline{C_{|F_{y_b}|}} = \frac{\overline{|F_{y_{blade}}|}}{0.5\rho S V^2} \tag{1}$$

Where $\overline{C_{F_x}}$ is the mean of total thrust coefficient over 360°, to be maximized, and $\overline{C_{|F_{y_b}|}}$ is the mean transverse blade force coefficient over 360°, to be minimized. In (1), S is the swept frontal area ($S = Dl$) and V the flume tank flow velocity. The objective function $\overline{C_{|F_{y_b}|}}$ is implemented here and considers that any transverse force generated individually by a blade is a loss of propeller efficiency.

Finally, the optimization problem to be solved for one operating point (fixed λ) is expressed as

$$\min_{\boldsymbol{x}\in\Omega} \; -\overline{C_{F_x}(\boldsymbol{x})}, \overline{C_{|F_{y_b}|}(\boldsymbol{x})} \tag{2}$$

Where $\boldsymbol{x} = (x_i)_{1\leq i\leq 4} \in \Omega \subset \mathbb{R}^4$ are design variables, to be determined, that define the blade pitch law, (θ_1,ϕ_1,θ_2,ϕ_2) for the trochoidal mode, or (θ_1,β_1,θ_2,β_2) for the cycloidal mode. The variability domain Ω, represented by blue and red rectangles on Figure 5, depends on each mode:

- Cycloidal mode : $\theta_1 \in [70°,160°]$, $\beta_1 \in [-100°,-30°]$, $\theta_2 \in [200°,290°]$ and $\beta_2 \in [10°,70°]$.
- Trochoidal mode : $\theta_1 \in [90°,160°]$, $\phi_1 \in [2°,60°]$, $\theta_2 \in [180°,260°]$ and $\phi_2 \in [-70°,-10°]$.

The evaluation of objective functions in (1) is performed with a multi-model approach, using both CFD and experimental measurements in the the flume tank. Indeed, a multi-fidelity efficient global optimization strategy is presently applied (see Section III).

III – Optimization method

We consider abstract optimization problems, where several objectives have to be minimized simultaneously over a design variable $\Omega \subset \mathbb{R}^d$:

$$\min_{\boldsymbol{x}\in\Omega} f_1(\boldsymbol{x}),\ldots,f_m(\boldsymbol{x}) \quad \text{s.t.} \quad \boldsymbol{g}(\boldsymbol{x}) \leq 0 \tag{3}$$

where $\boldsymbol{x} = (x_i)_{1\leq i\leq d}$ is a vector of design variables, $\boldsymbol{f} = (f_j)_{1\leq j\leq m}$ is a vector of objective functions to be minimized ($f_i : \Omega \mapsto \mathbb{R}$), and $\boldsymbol{g} = (g_k)_{1\leq k\leq p}$ is a vector of inequality constraints ($g_k : \Omega \mapsto \mathbb{R}$). The existence of an optimal solution, minimizing all objectives at once is usually not granted. This leads to the search for an optimal set of solutions, called the Pareto front. According to the Pareto domination rule [7], $\boldsymbol{x} \in \Omega$ is said dominated by $\boldsymbol{x'} \in \Omega$ if for all $1 \leq j \leq m$, $f_j(\boldsymbol{x'}) \leq f_j(\boldsymbol{x})$, and $\boldsymbol{g}(\boldsymbol{x'}) \leq 0$. The set of optimal (non-dominated) design vectors, to be determined in Ω, is then called the Pareto set. Evolutionary algorithms [3] have been shown to be well-adapted for solving multi-objective problems in real-word applications with moderate objective computation cost [8].

In the present work, individual evaluations of the objective functions are assumed to be very expensive. A common approach is then to use surrogate models in place of $\boldsymbol{f}$ to reduce the computational burden related to the evaluations of $\boldsymbol{f}$. Gaussian processes (GP) [17] are presently considered, which, owing to their statistical nature, provide for each objective function, both a prediction value and a measure of the uncertainty (variance) in this prediction. These features are appealing in the optimization context, as they can be exploited to derive rigorous optimization strategies, by evaluating sequentially the objective functions at design vectors that maximize a so-called merit function [16]. In mono-objective problems, GP-based approaches are globally referred to as Efficient Global Optimization (EGO) [9], where the merit function is based on an Expected Improvement (EI) criterion, expressing a trade-off between sampling in promising regions and exploring in unsampled regions. EGO has been successfully applied to complex optimization problems, such as non-linear fluid-structure interaction problems [19] or RANS computations [13].

Over the last few years, surrogate-based approaches have also been proposed to address the multi-objective problem. Indeed, several GP-based multi-objective optimization strategies propose to extend the EI infilling criterion of [9]. The definition of the improvement can then be considered over the Pareto front [22], using for instance, Maximin distance [21], Euclidean distance [10], or the well-known Hypervolume infilling criterion [4]. In particular, [14] have proposed and validated, on a real-word composite panel application, the efficiency of a new merit function: Minimization of the Variance of the Predicted Front.

When objective functions are evaluated using complex computational tools, it is typically feasible to define a series of models with different levels of fidelity and computational costs to estimate their values. For example, the fidelity levels might correspond to finite element models with varying mesh refinements, resulting in differences in computational cost and accuracy. Thus, the global computational cost of the optimization can be reduced by using such different models in a multi-fidelity (MF) EGO framework [20]. In the present work, the blade pitch law optimization problem is solved by using a multi-fidelity, multi-objective EGO approach.

In Section III – 1, we summarize the construction of a GP model for an objective function f_j. Section III – 2 provides the extension of the GP surrogate construction to the multi-fidelity case. Finally, definitions of multi-objective surrogate-based merit functions, that are used in the present work, are provided in Section III – 3.

III – 1 GP surrogate construction

In the present Section III – 1, the GP surrogate construction of an objective function f_j is provided. The method is exactly the same for the GP surrogate construction of an inequality constraint function g_k.

We consider a set of n training points $\mathcal{X} = (\boldsymbol{x}_1, \ldots, \boldsymbol{x}_n)$, each in Ω. The training points are associated to the vector $\mathcal{Y}^{(j)} = (y_1^{(j)}, \ldots, y_n^{(j)})$ of noisy observations of the objective function f_j. It is assumed that $y_i^{(j)} = f_j(\boldsymbol{x}_i) + \epsilon_i^{(j)}$, where the $\epsilon_i^{(j)}$ are independent and identically distributed Gaussian random variables having zero-mean and variance $\sigma_{\epsilon_j}^2$.

The GP construction considers that $f_j(\boldsymbol{x})$ is a realization of a zero-mean multivariate Gaussian process with covariance function C_j. We consider here the multidimensional squared exponential covariance functions defined by

$$C_j(\boldsymbol{x},\boldsymbol{x}';\Theta_j) \doteq \theta_1 \prod_{i=1}^{d} \exp\left(\frac{-(x_i - x_i')^2}{2l_i^2}\right) + \theta_2 \tag{4}$$

where $\Theta_j = \left(\theta_1^{(j)}, \theta_2^{(j)}, l_1^{(j)}, \ldots, l_d^{(j)}\right)$ is the vector of covariance hyper-parameters to be inferred from the $\mathcal{Y}^{(j)}$ observations. From the conditional rules of joint Gaussian distributions [17], the *best* prediction $\widehat{f}_j(\boldsymbol{x})$ of $f_j(\boldsymbol{x})$, *i.e.* the mean of $y^{(j)}$, and the prediction variance $\widehat{\sigma}_j^{\,2}(\boldsymbol{x})$ are given by,

$$\widehat{f}_j(\boldsymbol{x}) = \boldsymbol{k}_j^{\mathrm{T}}(\boldsymbol{x}) \left(\boldsymbol{C}_j(\Theta_j) + \sigma_{\epsilon_j}^2 \boldsymbol{I}\right)^{-1} \mathcal{Y}^{(j)} \tag{5}$$

$$\widehat{\sigma}_j^{\,2}(\boldsymbol{x}) = \kappa_j(\boldsymbol{x}) + \sigma_{\epsilon_j}^2 - \boldsymbol{k}_j^{\mathrm{T}}(\boldsymbol{x}) \left(\boldsymbol{C}_j(\Theta_j) + \sigma_{\epsilon_j}^2 \boldsymbol{I}\right)^{-1} \boldsymbol{k}_j(\boldsymbol{x}) \tag{6}$$

In (5) and (6) we have denoted $\boldsymbol{C}_j \in \mathbb{R}^{n\times n}$ the symmetric covariance matrix of the training points, $\kappa_j(\boldsymbol{x}) \doteq C_j(\boldsymbol{x},\boldsymbol{x};\Theta_j)$, $\boldsymbol{k}_j(\boldsymbol{x}) \doteq (C_j(\boldsymbol{x},\boldsymbol{x}_1;\Theta_j) \cdots C_j(\boldsymbol{x},\boldsymbol{x}_n;\Theta_j))^{\mathrm{T}}$ the covariance vector between the observations in $\mathcal{X}$ and $\boldsymbol{x}$, and $\boldsymbol{I}$ the identity matrix of $\mathbb{R}^n$. The hyper-parameters Θ_j and noise variance $\sigma_{\epsilon_j}^2$ can be determined by maximizing the log-marginal likelihood (see [17] for more details).

III – 2 Multi-fidelity GP surrogate construction

In the present Section III – 2, the multi-fidelity GP surrogate construction of an objective function f_j is provided. Similar to the single-fidelity case (Section III – 1), the method is the same for the multi-fidelity GP surrogate construction of an inequality constraint function g_k.

We consider the availability of a sequence of L models $f_j^{(1)}, \ldots, f_j^{(\mathrm{L})}$ of increasing fidelity for the evaluation of objective functions, such that $f_j^{(l)}(\boldsymbol{x}) \xrightarrow{l\to\mathrm{L}} f_j(\boldsymbol{x}), \forall \boldsymbol{x} \in \Omega$. The computational cost associated to the evaluation of $f_j^{(l)}(\boldsymbol{x})$ increases with the fidelity level l, and the objective of the MF-surrogate is to incorporate observations corresponding to fidelity levels $l < \mathrm{L}$, to improve the predictive capability of the surrogate model of $f_j^{(\mathrm{L})}(\boldsymbol{x})$.

The recursive formulation proposed in [11], that breaks down the determination of the MF-surrogate in successive GP process constructions for each intermediate level, is presently used in the non-nested formulation of [20]. The key idea is to define the MF-surrogate at level l, denoted $Y_j^{(l)}$, as a correction of the MF-surrogate at level $l-1$. Specifically, we write for $l = 1, \ldots, \mathrm{L}$

$$Y_j^{(l)}(\boldsymbol{x}) = \rho_j^{(l-1)} Y_j^{(l-1)}(\boldsymbol{x}) + \delta Y_j^{(l)}(\boldsymbol{x}), \quad Y_j^{(0)}(\boldsymbol{x}) = 0 \tag{7}$$

where $\rho_j^{(l-1)} \in \mathbb{R}$ accounts for the correlation between the two successive levels, and $\delta Y_j^{(l)}(\boldsymbol{x})$ is the Gaussian correction process orthogonal to $Y_j^{(l-1)}(\boldsymbol{x})$. The MF-surrogate $Y_j^{(l)}$ is then a GP that dependents on the previous level MF-surrogate and on the noisy observations of $f_j^{(l)}(\boldsymbol{x})$, that is $\left[Y_j^{(l)}(\boldsymbol{x})|Y_j^{(l-1)}(\boldsymbol{x}), \mathcal{Y}_j^{(l)}\right] \sim \mathcal{N}\left(\widehat{f}_j^{\,(l)}(\boldsymbol{x}), \widehat{\sigma}^2_{j_{(l)}}(\boldsymbol{x})\right)$, with mean and variance respectively given by,

$$\widehat{f}_j^{\,(l)}(\boldsymbol{x}) = \rho_{j_{(l-1)}} \widehat{f}_j^{\,(l-1)}(\boldsymbol{x}) + \boldsymbol{k}^{\mathrm{T}}_{j_{(l)}}(\boldsymbol{x}) \left(\boldsymbol{C}_{j_{(l)}} + \sigma^2_{\epsilon_{j_{(l)}}} \boldsymbol{I}_{n_{(l)}}\right)^{-1} \Delta\mathcal{Y}_j^{(l)}(\rho_{j_{(l-1)}}) \tag{8}$$

$$\widehat{\sigma}^2_{j_{(l)}}(\boldsymbol{x}) = \rho^2_{j_{(l-1)}} \widehat{\sigma}^2_{j_{(l-1)}}(\boldsymbol{x}) + \kappa_{j_{(l)}}(\boldsymbol{x}) + \sigma^2_{\epsilon_{j_{(l)}}} - \boldsymbol{k}^{\mathrm{T}}_{j_{(l)}}(\boldsymbol{x}) \left(\boldsymbol{C}_{j_{(l)}} + \sigma^2_{\epsilon_{j_{(l)}}} \boldsymbol{I}_{n_{(l)}}\right)^{-1} \boldsymbol{k}_{j_{(l)}}(\boldsymbol{x}) \tag{9}$$

where $\Delta\mathcal{Y}_j^{(l)}$ is the vector of predicted residuals at training points and defined as

$$\Delta\mathcal{Y}_j^{(l)}(\rho_{j_{(l-1)}}) = \begin{cases} \mathcal{Y}_j^{(l)}, & l = 1 \\ \mathcal{Y}_j^{(l)} - \rho_{j_{(l-1)}} \widehat{f}_{j\,(l-1)}(\boldsymbol{x} \in \mathcal{X}^{(l)}), & l \geq 1 \end{cases} \tag{10}$$

As in the single-fidelity case, the hyper-parameters of level l are selected by maximizing the log-marginal likelihood of $Y_j^{(l)}$ (see [17] or [11] for more details).

III – 3 Merit functions

Surrogate-based optimization methods rely on the sequential construction of statistical surrogate models, using training sets of computed objective and constraint function values, that are refined according to a prescribed infilling strategy [16]. At each iteration of the iterative surrogate-based optimization, a new design vector $\boldsymbol{x}_{n+1}$ is thus added to $\mathcal{X}$, and finally $\boldsymbol{f}$ and $\boldsymbol{g}$ are computed. A new iteration can then start by updating surrogate models, and the iterative process is repeated until a stopping criterion is satisfied or the resources allocated to the optimization have been exhausted.

In the case of a multi-fidelity surrogate-based optimization, the fidelity level l_* of the model to be evaluated should also be determined [20]. In the present work, objective functions are evaluated from CFD and experiments (high fidelity level). This multi-model framework allows the construction of MF surrogates to reduce the global cost of the surrogate-based optimization. Due to CFD costs (several hours for one design vector) and the availability of experimental equipment, an optimization that includes the selection of the fidelity level during EGO iterations [20] is not possible here. Consequently, optimizations based on CFD models have been carried out prior to the experimental campaign. This made it possible to identify the cases of interest for the experiments, then during the experimental campaign, optimizations have been carried out by evaluating only the highest fidelity level L (experiments), while exploiting the CFD calculations in multi-fidelity surrogate models.

Similar to the previous work of authors [6], two new design vectors are determined and added to $\mathcal{X}$ at each new iteration of the iterative surrogate-based optimization. Specifically, the Minimization of the Variance of the Predicted Front [14] and Expected Improvement Matrix Hypervolume criterion [23] criteria are considered to allow respectively, the reduction of the uncertainty of the predicted Pareto front and the improvement of the computed Pareto front (see [6] for more details).

IV – Results and discussion

A total of six multi-fidelity optimizations have been carried out during experiments in the Ifremer flume tank at Boulogne-sur-Mer on May 2024. For some optimizations performed over two consecutive days, the evaluation of an optimized pitch law is duplicated to ensure measurement repeatability.

Section IV – 1 highlights first the interest of using different fidelity levels by comparing two approaches:

- Single-fidelity optimization approach with the CFD model;
- Multi-fidelity optimization approach with CFD and experimental models.

Section IV – 2 presents global optimization results for both cycloidal and trochoidal parameterizations at $\lambda \in \{0.2, 0.375, 0.5\}$.

IV – 1 Multi-fidelity process interest

Figure 6 shows the results from the arbitrary cycloidal optimization at $\lambda = 0.5$. Left graph shows Pareto fronts on the objective space. Red squares correspond to CFD evaluations of objective functions $\overline{C_{F_x}}$ and $\overline{C_{|F_{y_b}|}}$, sequentially determined with a single-fidelity EGO optimization. The associated predicted Pareto front, at convergence, is given by red circles. Experimental evaluations of objective functions are blues filled triangles, also sequentially determined with an EGO optimization, but using multi-fidelity surrogates (CFD and experiments). Hollow blue triangles are experimental evaluations of objective functions, obtained from the sampling step and using a Latin Hypercube Sampling (LHS) method. Finally, the multi-fidelity predicted Pareto fronts, after the sampling step and at convergence, are given by blue hollow and filled circles respectively. It can thus be

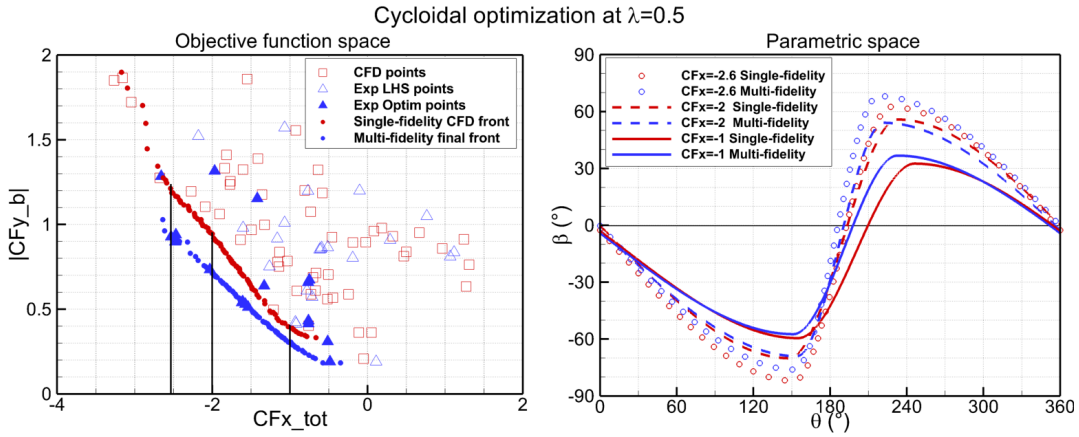

Figure 6: Comparison of the single-fidelity and multi-fidelity results at cycloidal $\lambda = 0.5$ mode on the predicted Pareto fronts (left) and on the parametric space (right).

observed in Figure 6 that the two fidelity levels are very close for the prediction of the Pareto front with respect to $\overline{C_{F_x}}$. For $\overline{C_{|F_{y_b}|}}$, regarding the Pareto front, the objective is slightly overestimated by the CFD. This result is, in principle, consistent, in the sense that the cycloidal mode involves a more complex flow physics to model, with very rapid dynamics, including vortex shedding during the blade reversal. The advantage of the multi-fidelity approach is evident here, as the recursive construction of surrogate models allows for the correction of the higher-fidelity prediction.

At the right, the graph presents the optimal pitching laws generated by the points on the Pareto fronts from both single and multi-fidelity at the three values of $\overline{C_{F_x}}$ (represented by vertical black lines on the left graph). This second figure reflects the location of the Pareto front points on the parametric space. The figure shows that along the three locations on the fronts, optimal laws are very similar in terms of amplitude and phase despite the gap on the Pareto fronts. This result demonstrates that even if the Pareto fronts appear different between single and multi-fidelity, the optimal points are gathered at the same locations in the parametric domain.

IV – 2 Global results

This section presents results of optimization for three values of λ with both cycloidal and trochoidal parameterization methods. In Figure 7, cycloidal predicted Pareto fronts are represented by hollow diamond scatters, whereas trochoidal predicted fronts are represented by filled square scatters. Colors represent the three λ operating point (green for $\lambda = 0.2$, blue for $\lambda = 0.375$ and red for $\lambda = 0.5$). The upper right frame shows more precisely $\lambda = 0.375$ and $\lambda = 0.5$ predicted fronts. Finally, conventional symmetric pitching laws (with eccentricity definition for cycloidal mode and sinusoidal for trochoidal mode) are also represented as colored single points.

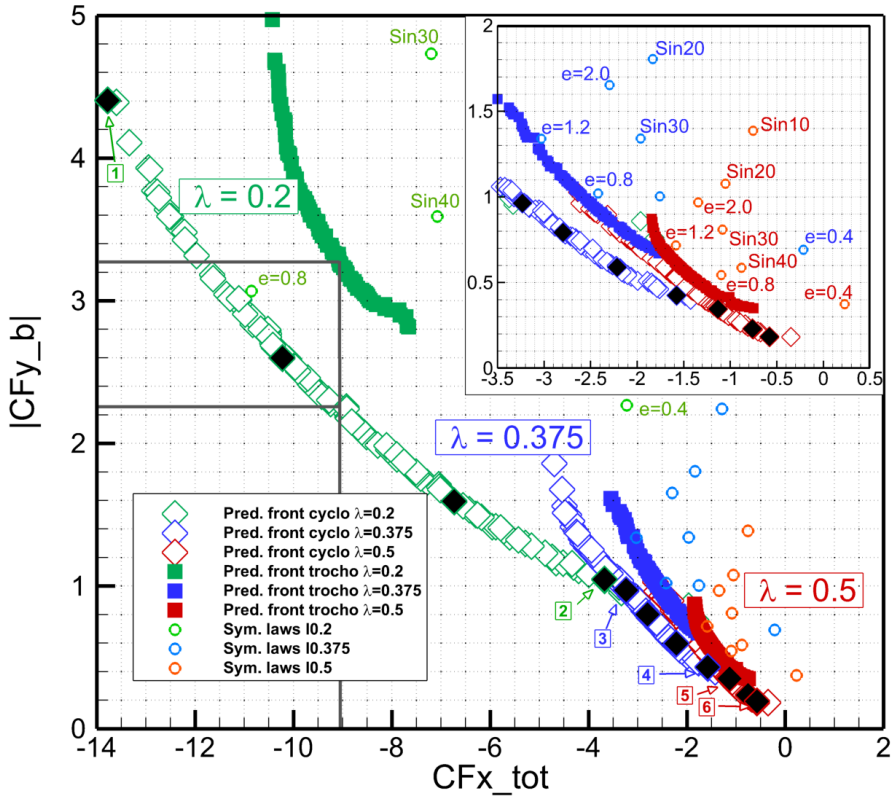

Figure 7: Pareto fronts obtained after multi-fidelity optimizations for various λ values.

Predicted Pareto fronts demonstrate that cycloidal mode is more effective in terms of thrust gain and side force diminution than trochoidal motion for all three low advance parameters. However, the gap becomes less pronounced for $\lambda = 0.5$ case. The capacities of cycloidal mode is also higher than trochoidal mode: the Pareto front is wider and more extended, especially for the case $\lambda = 0.2$. Figure 7 also proves than optimized pitching law are more efficient than traditional symmetric laws in both modes (as discussed in previous work [6]), because of the asymmetry upstream/downstream pitching laws.

Figure 8 shows the temporal evolution of the force signals over one rotation for a cycloidal and a trochoidal pitching to explain the gap between the two modes on the predicted fronts at $\lambda = 0.2$. The results are extracted from experimental points closed to the both fronts for which the total mean thrust is equal to $\overline{C_{F_x}} = -9$ (represented by the vertical black line on Figure 7).

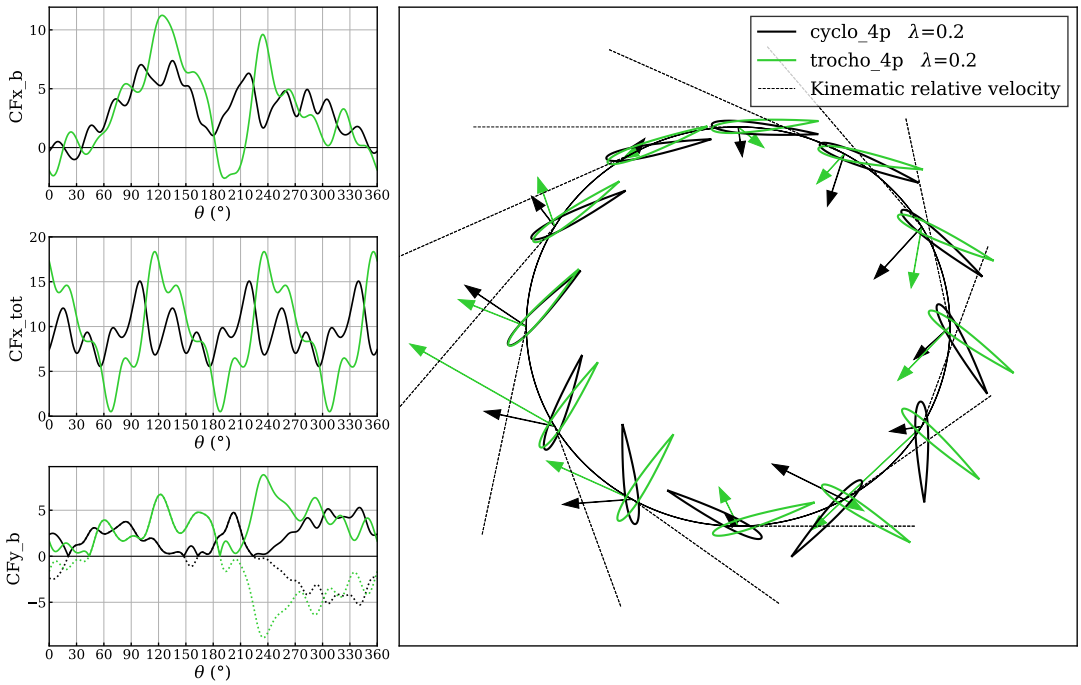

Figure 8: Temporal force signal comparison between trochoidal and cycloidal optimization at $\lambda = 0.2$.

At the left, graphs illustrate respectively the single blade thrust coefficient, total thrust coefficient and blade side force coefficient. The side force is represented in absolute value (from which the second objective is calculated as the mean of the absolute value) and in normal value in dotted line to compare the variations of the signal. The right graph displays the blade pitch angles sampled every $\theta = 30°$ along the rotor. The $\theta = 0°$ position is at the North whereas $\theta = 90°$ is at the West. Arrows indicate the total force (vectorial sum of thrust and side force) at each positions. Lastly, dashed black lines represent relative kinematic velocity directions at each positions. This kinematic velocity is defined as the vectorial sum of the advance speed and the peripheral speed. The main comment is that concerning the thrust, the mean value of the total thrust is the same whereas the variation is significantly higher for the trochoidal mode at λ=0.2. The blade thrust coefficient shows a large increase at $\theta = 120°$ of the signal for the trochoidal pitch law in comparison with the cycloidal pitch law. This increase of thrust comes with an increase of the side force at $\theta = 120°$ which is also observed on the total hydrodynamic force on the right graph at this position. This can be explain by the fact that at this position the trochoidal blade motion has an higher incidence angle considering the kinematic relative velocity. The position $\theta = 210°$ presents also an interesting comparison. Whereas cycloidal blade is nearly aligned with the kinematic velocity, the trochoidal blade becomes perpendicular to the relative flow is thus a large drag appears especially at $\theta = 240°$ which causes mainly a large side force.

To summarize this comparison, at λ=0.2 (and generally at low λ values), the trochoid motion is mush less aligned with the relative flow direction, even with an optimized

motion, and generates higher hydrodynamic loads which highly impact the alternative blade load variation.

Lastly, Figure 9 presents the optimized pitch laws from several point of interest of the cycloidal Pareto fronts from the Figure 7, highlighted in black. These points provide a continuous sampling of the optimal pitching laws when we decrease the $\overline{C_{F_x}}$ traveling through the cycloidal fronts. Indeed, the optimal law referred as n°1 is the upper left point of the Pareto front at $\lambda = 0.2$. The n°2 optimal law is the lower right point of the Pareto front at $\lambda = 0.2$. The two additional black diamonds on the λ=0.2 Pareto front are the two intermediate green laws in Figure 9. Similarly, n°3 and n°4 optimal laws are the two extremes points of the $\lambda = 0.375$ cycloidal Pareto front as the n°5 and n°6 for $\lambda = 0.5$. Figure 9 also display the symmetrical law with eccentricity formulation, $e = 0.8$, in dashed black lines.

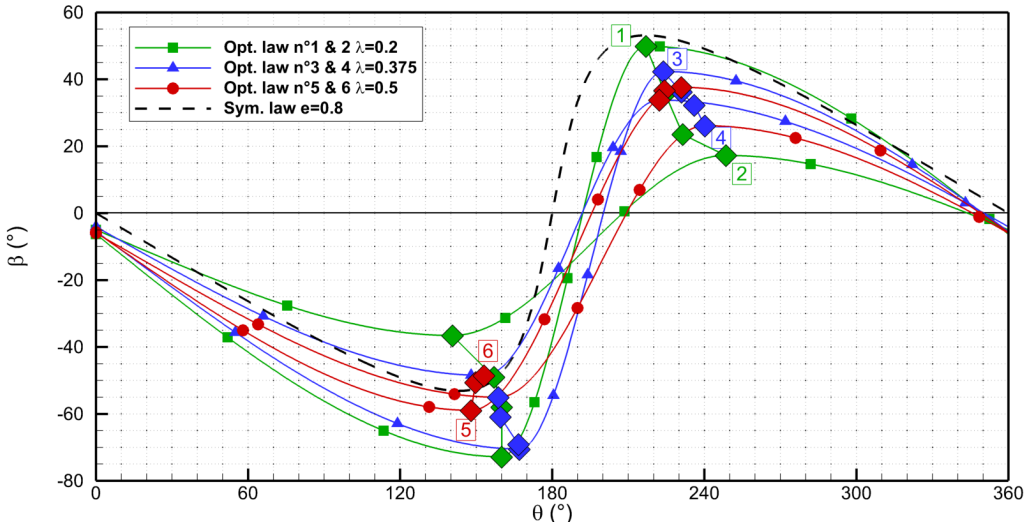

Figure 9: Variation of the optimized pitching laws along all the Pareto fronts.

This figure strongly highlights the asymmetry of optimized pitching laws in comparison with the $e = 0.8$-symmetrical law: for almost all optimized laws the upstream portion has a larger amplitude than the $e = 0.8$-symmetrical law, whereas the downstream portion has a lower amplitude. The blade reversal (when β crosses the 0-line) is also shifted towards later than $\theta = 180°$ positions for all optimized pitching laws. This special feature has also being observed previously in [6].

For each λ optimization, two generic trends can be observed for all optimal parameters: more the required thrust is high and more is the amplitude and more closer are the two central control points. Yet, these trends are less pronounced for the $\lambda = 0.5$ optimization. Nevertheless, this pitch law study provides an important feedback for the operation of cycloidal propeller at low advance parameter: the pitch law shape has a major impact on the thrust generated with respect of optimal low side-force.

V – Conclusion

This paper presents an innovative multi-fidelity optimization of a cycloidal propeller blade pitch laws with both numerical and experimental fidelity models. Indeed, according to previous study, optimization of blade pitching laws shows huge benefits from conventional symmetrical of traditional cycloidal propellers.

First results of optimization show that the final Pareto front from the multi-fidelity layer is slightly different that the single-fidelity Pareto front for $\overline{C_{|F_{y_b}|}}$ objective. This is explained by the fact that the single-fidelity process, the numerical CFD model, has a lower prediction of complex flow physics than experiments. Nevertheless, the recursive construction of surrogate models on the multi-fidelity process takes advantage of the high fidelity level correction on the performances prediction. And even if multi-fidelity show a slight difference on the Pareto front results, the predicted final optimal laws remain similar that gives the optimization process confidence.

Global results for the optimizations at the three λ values provide many interesting findings. First of all, cycloidal mode at low λ values overtakes trochoidal mode for both objectives. Pareto fronts also show a wider area for cycloidal mode which allows a larger capacity of changing thrust. The differences come from the incidence angle which is more adapted for cycloidal laws than trochoidal laws at low λ, even with a parameterized formulation. But more λ is closer to one and more the gap between cycloidal and trochoidal modes reduces. Secondly, all the optimized pitching laws measured in experiments surpass the conventional symmetric law performances, either in cycloidal or trochoidal motion. This result principally comes from the faculty of dissymmetry the pitching law, with a larger amplitude in the upstream phase and a lower amplitude in the downstream phase than a symmetrical pitching law. Finally, the last finding concerns the way the optimized law are changing along the Pareto fronts when we change the thrust. The amplitude of optimal laws decreases as the required thrust increases. This evolution of the optimal laws regarding the need in thrust at low λ values reveals the requirement of changing the law to change the operation of the propulsor, at least for low λ values.

Perspectives concern the continuation of the optimization for $\lambda > 1$ and to determine the optimal value to change from cycloidal to trochoidal mode (when the Pareto fronts are overlapping). Authors will also investigate the use of lower fidelity model than CFD, such as potential code [15], to explore other parameters as the propeller geometry (number of blades, solidity, etc...). The final goal of cycloidal pitch law optimization study is to implement a real time algorithm method for which the instrumented propeller can adapt itself the pitch law according the incoming flow it experiences (under different conditions such as the tidal effects, with leeway or under slipping for wind propulsive system combination).

References

[1] S. Abbaszadeh, S. Hoerner, T. Maître, and R. Leidhold. Experimental investigation of an optimised pitch control for a vertical-axis turbine. *IET Renewable Power Generation*, 13(16):3106–3112, 2019.

[2] J.-E. Bartels and D. Jürgens. The voith schneider propeller: Current applications and new developments. *Heidenheim: Voith Publication*, 2006.

[3] K. Deb, A. Pratap, S. Agarwal, and T. Meyarivan. A fast and elitist multiobjective genetic algorithm: Nsga-ii. *IEEE transactions on evolutionary computation*, 6(2):182–197, 2002.

[4] M. T. Emmerich, A. H. Deutz, and J. W. Klinkenberg. Hypervolume-based expected improvement: Monotonicity properties and exact computation. In *2011 IEEE Congress of Evolutionary Computation (CEC)*, pages 2147–2154. IEEE, 2011.

[5] G. Fasse, F. Becker, F. Hauville, J.-A. Astolfi, and G. Germain. An experimental blade-controlled platform for the design of smart cross-flow propeller. *Ocean Engineering*, 250:110921, 2022.

[6] G. Fasse, M. Sacher, F. Hauville, J.-A. Astolfi, and G. Germain. Multi-objective optimization of cycloidal blade-controlled propeller: An experimental approach. *Ocean Engineering*, 299:117363, 2024.

[7] C. M. Fonseca and P. J. Fleming. Multiobjective optimization and multiple constraint handling with evolutionary algorithms. i. a unified formulation. *IEEE Transactions on Systems, Man, and Cybernetics-Part A: Systems and Humans*, 28(1):26–37, 1998.

[8] R. Huang, X. Luo, B. Ji, P. Wang, A. Yu, Z. Zhai, and J. Zhou. Multi-objective optimization of a mixed-flow pump impeller using modified nsga-ii algorithm. *Science China technological sciences*, 58(12):2122–2130, 2015.

[9] D. R. Jones, M. Schonlau, and W. J. Welch. Efficient Global Optimization of Expensive Black-Box Functions. *Journal of Global optimization*, 13(4):455–492, 1998.

[10] A. J. Keane. Statistical improvement criteria for use in multiobjective design optimization. *AIAA journal*, 44(4):879–891, 2006.

[11] L. Le Gratiet and J. Garnier. Recursive co-kriging model for Design of Computer experiments with multiple levels of fidelity. *International Journal for Uncertainty Quantification*, 4(5):365–386, 2014.

[12] W. Liu, Z. Liu, Q. Chen, and C. Ma. Research on efficiency optimization of the voith-schneider propeller based on motion curve parameter control. *Ocean Engineering*, 299:117136, 2024.

[13] M. Meliani, N. Bartoli, T. Lefebvre, M.-A. Bouhlel, J. Martins, and J. Morlier. Multi-fidelity efficient global optimization : Methodology and application to airfoil shape design. In *AIAA Aviation 2019 Forum,Dallas, United States*, 2019.

[14] A. G. d. Passos and M. A. Luersen. Multiobjective optimization of laminated composite parts with curvilinear fibers using kriging-based approaches. *Structural and Multidisciplinary Optimization*, 57(3):1115–1127, 2018.

[15] P. Perali, M. Sacher, J.-B. Leroux, J. Wackers, B. Augier, F. Hauville, and P. Bot. Performance prediction of a hydrofoil near the free surface using low (bem) and high (rans) fidelity methods. *Applied Ocean Research*, 151:104157, 2024.

[16] V. Picheny, T. Wagner, and D. Ginsbourger. A benchmark of kriging-based infill criteria for noisy optimization. *Structural and Multidisciplinary Optimization*, 48(3):607–626, Sep 2013.

[17] C. E. Rasmussen and C. K. I. Williams. *Gaussian Processes for Machine Learning*. MIT Press, 2006.

[18] B. T. Roesler, M. Francsiquez, and B. P. Epps. Design and analysis of trochoidal propulsors using nonlinear programming optimization techniques. In *International Conference on Offshore Mechanics and Arctic Engineering*, volume 45516, page V08BT06A032. American Society of Mechanical Engineers, 2014.

[19] M. Sacher, F. Hauville, R. Duvigneau, O. Le Maître, N. Aubin, and M. Durand. Efficient optimization procedure in non-linear fluid-structure interaction problem: Application to mainsail trimming in upwind conditions. *Journal of Fluids and Structures*, 69:209 – 231, 2017.

[20] M. Sacher, O. Le Maître, R. Duvigneau, F. Hauville, M. Durand, and C. Lothodé. A non-nested infilling strategy for multifidelity based efficient global optimization. *International Journal for Uncertainty Quantification*, 11(1), 2021.

[21] J. D. Svenson and T. J. Santner. Multiobjective optimization of expensive black-box functions via expected maximin improvement. *The Ohio State University, Columbus, Ohio*, 32, 2010.

[22] T. Wagner, M. Emmerich, A. Deutz, and W. Ponweiser. On expected-improvement criteria for model-based multi-objective optimization. In *International Conference on Parallel Problem Solving from Nature*, pages 718–727. Springer, 2010.

[23] D. Zhan, Y. Cheng, and J. Liu. Expected improvement matrix-based infill criteria for expensive multiobjective optimization. *IEEE Transactions on Evolutionary Computation*, 21(6):956–975, 2017.